Editors' Suggestion

Unit-cell-thick domain in free-standing quasi-two-dimensional ferroelectric material

Yuwei Guo,[1] Berit Goodge,[2,3] Lifu Zhang,[1] Jie Jiang,[1] Yu Chen,[4] Lena F. Kourkoutis,[2,3] and Jian Shi[1,5,*]

[1]*Department of Materials Science and Engineering, Rensselaer Polytechnic Institute, Troy, New York 12180, USA*
[2]*School of Applied and Engineering Physics, Cornell University, Ithaca, New York 14853, USA*
[3]*Kavli Institute at Cornell for Nanoscale Science, Ithaca, New York 14853, USA*
[4]*Department of Computer Science, Rensselaer Polytechnic Institute, Troy, New York 12180, USA*
[5]*Center for Materials, Devices, and Integrated Systems, Rensselaer Polytechnic Institute, Troy, New York 12180, USA*

(Received 6 October 2020; revised 18 February 2021; accepted 24 March 2021; published 12 April 2021)

Two-dimensional (2D) and quasi-2D ferroelectric materials have demonstrated their potential for enabling device miniaturization. The fundamental understanding of the ferroelectric domain structure at atomic scale is limited, however, hindering development of functional device units at the microscopic level. In this paper, we employ a Dion–Jacobson layered oxide $CsBiNb_2O_7$ (CBNO), which has been predicted to be ferroelectric with high Curie temperature and large in-plane polarization, as a model system to study its ferroelectric domain structure with atomic scale analysis. We reveal the existence of unit-cell-thick ferroelectric domain size as well as both 180° and 90° domain walls in free-standing CBNO. In an epitaxial CBNO film grown on a $LaAlO_3$ substrate, we discover multiple stacking structures resembling the Aurivillius and the Ruddlesden–Popper phases. We also analyze the interfacial dislocations and their associated lattice distortion fields in the epitaxial film. This paper may inspire design concepts for ferroelectric devices demanding unit-cell-thick domain size.

DOI: 10.1103/PhysRevMaterials.5.044403

I. INTRODUCTION

Ferroelectric materials are of great interest in their applications to many electronic devices, for example, non-volatile high-density memories [1], ultra-fast switchings [2], and thin film capacitors [3]. To keep increasing the integration density of these devices following Moore's law, atomic-scale domains enabling device miniaturization is of great significance. For instance, in ferroelectric devices whose working principle is associated with far-field switching of dipole moment [4], the domain size of electrodeless film directly influences the performance of the device [5,6]. Smaller ferroelectric domain size, namely, more ferroelectric domains per ferroelectric device, enables more memory states [7,8], which are highly demanded for synapselike devices. Thus, fundamental understanding of the intrinsic domain structure of free-standing two-dimensional (2D) and quasi-2D materials is important in the design of synaptic devices with a large number of synaptic states. In fact, partially due to this reason, researchers have spent enormous efforts on understanding the domain structure of electrodeless atomic-thick or a few-layer-thick SnTe [9], $BiFeO_3$ [10], In_2Se_3 [11], and $CuInP_2S_6$ [12] ferroelectric materials. Due to the increased depolarization fields in ferroelectric materials with reduced dimension, however, a domain size of a few nanometers is rare [9,13–15]. For instance, in $BaTiO_3$ and $BiFeO_3$ films, the typical domain size ranges from tens to hundreds of nanometers [16,17]. Under certain scenarios, the domain size can be engineered to a few nanometers. For example, when $BaTiO_3$ is in the nanocrystal morphology with a particle diameter of 8 nm, its ferroelectric domain size can be approximately 5 nm by colloidal morphology control [6].

Domain wall energy plays an important role in determining the domain size. Domain wall energy includes three terms: dipolar energy, anisotropy energy, and elastic energy [18–20]. The anisotropy energy is negligible in ferroelectrics since the polarization directions barely deviate from the ferroelectric axis. Polarization magnitude, on the other hand, can vary from its spontaneous value within the domain wall, so the lattice needs to assume certain piezoelectric strains that correspond to the particular polarization states. In a layered quasi-2D ferroelectric material, the piezoelectric strain is smaller than most typical perovskite oxides ($BaTiO_3$, $PbTiO_3$, $BiFeO_3$, etc.) due to the weak bonding along the layer stacking direction resulting from the large d spacing between neighboring atomic layers [20]. Consequently, the elastic energy resulting from the piezoelectric strains in quasi-2D materials is smaller than that in conventional three-dimensional perovskites. The dipolar energy is proportional to the square of the polarization gradient across the domain wall, so a larger lattice constant along the stacking direction in quasi-2D materials may also decrease the dipolar energy contribution to the domain wall if the domain wall normal is along the layer stacking direction. Overall, the reduced domain wall energy in quasi-2D materials may increase the density of domain walls, leading to smaller domain sizes. It has been reported that, in 2D SnTe, ferroelectric domains down to 1 unit-cell [9] are observed. As a quasi-2D material, the interaction between layers along the c axis direction in $CsBiNb_2O_7$ (CBNO) is weak. Such a weak interaction may be a possible reason leading to atomically thick domains, in some analogy to the case of SnTe crystals.

We propose a representative quasi-2D ferroelectric material, CBNO, to study its ferroelectric domain structure at

*Corresponding author: shij4@rpi.edu

atomic scale. As a Dion–Jacobson layered oxide, CBNO has been predicted to possess a large in-plane polarization ($\sim$40 C/cm^2) along the *a* axis, mainly attributed to the non-centrosymmetric position of Bi^{3+} relative to its neighboring O^{2-} ions [21,22]. A high Curie temperature of about 1033 °C has also been predicted for CBNO [23]. Additionally, CBNO has been proposed to be an excellent ferroelectric Rashba–Dresselhaus wide band gap semiconductor with persistent spin helix due to the presence of heavy Bi atoms [24,25]. To design ferroelectric devices with small domain sizes and explore their rich material physics, a fundamental understanding of the domain structure of CBNO is necessary and also of broad interest to the research community of ferroelectric materials.

In this paper, we prepare both free-standing CBNO films and epitaxial CBNO films on $LaAlO_3$ substrates by molten-salt assisted synthesis (see Methods). Employing aberration-corrected scanning transmission electron microscopy (Cs-STEM), we reveal domain sizes down to 1 unit-cell with 180° domain walls in free-standing CBNO, as well as change in domain orientations around a 90° domain wall. In addition, we discover multiple stacking structures and interfacial dislocations in epitaxial CBNO films and analyze the strain fields around the dislocations by geometric phase analysis (GPA). The observation of the absence of defects, such as stacking faults and dislocations, in free-standing CBNO confirms that the growth conditions are appropriate. Thus, the possible defects brought from the epitaxial process could be attributed to the substrate effect. Taken together, this paper demonstrates the exceptionally narrow ferroelectric domains and domain walls in a quasi-2D oxide that leads to an emergent material category for potential high integration density devices.

II. METHODS

A. Growth of free-standing films

Free-standing CBNO membranes were grown by molten-salt assisted synthesis [26]. Powder precursors of Cs_2CO_3 (Sigma-Aldrich, 99%), Bi_2O_3 (Sigma-Aldrich, 99.9%), and Nb_2O_5 (Sigma-Aldrich, 99.9%) with a molar ratio of 3:2:4 were finely ground together with CsCl salt (Sigma-Aldrich, 99.9%) before they were then loaded in an alumina crucible. The weight of CsCl salt was 10 times the weight of all the other precursors. The crucible was heated in a horizontal furnace in open air and underwent three temperature ranges. First, the temperature increased to 900 °C with a ramp rate of 225 °C/h. Second, the crucible was held at 900 °C for another 4 h. Lastly, it was cooled down slowly at a rate of 2 °C/min. CBNO square crystals of millimeter size and thickness of about 0.2 mm were formed in the crucible and then cleaned with deionized water. Exfoliation of the CBNO single crystal was conducted by the scotch tape method. Thin membranes of CBNO were then transferred onto transmission electron microscopy (TEM) grid or *c*-plane sapphire substrate for further focused ion beam (FIB) preparation.

B. Growth of epitaxial CBNO film on $LaAlO_3$ substrate

$LaAlO_3$ substrate (MTI Corporation) was sequentially cleaned with acetone, ethanol, and deionized water in an ultrasonic bath for 5 min each and then blown to dry. The precursors were the same with that used to grow free-standing CBNO. The weight ratio of CsCl salt (Sigma-Aldrich, 99.9%) and all the other precursors was 10:1. All the precursors and CsCl salt were put into an alumina crucible in which $LaAlO_3$ substrates are placed horizontally. The temperature of the crucible was controlled by an open-end horizontal furnace. It was first increased to 200 °C and held for 2 h to remove residue water in all powders. Secondly, the temperature was increased to 600 °C and held for another 2 h to allow full decomposition of Cs_2CO_3 into Cs_2O. Thirdly, the crucible was heated up to 900 °C at a ramp rate of 5 °C/min. After 4 h of 900 °C growth, the crucible was cooled down to room temperature at a rate of 2 °C/min. Comparing with Cs components, i.e., Cs_2CO_3, Cs_2O, and CsCl, Bi_2O_3 and Nb_2O_5 have lower saturation, so their undissolved powders remain at the bottom of the crucible. As Bi^{3+} and Nb^{5+} ions are consumed during the formation of CBNO, these powders start to dissolve slowly again and result in a higher concentration of Bi^{3+} and Nb^{5+} at the bottom of the crucible where the $LaAlO_3$ substrates present. Thus, the nonuniform solution of the precursors may result in Cs deficiency in CBNO film grown on $LaAlO_3$ substrate.

C. Microscopy sample preapation, imaging, and analysis

A Helios G4 UX FIB was employed to prepare the cross-sectional TEM sample of the free-standing CBNO film transferred onto a *c*-plane sapphire substrate and the cross-sectional TEM sample of an epitaxial CBNO film grown on a $LaAlO_3$ substrate. TEM images of the epitaxial CBNO-$LaAlO_3$ sample and its electron diffraction patterns were obtained at room temperature with an FEI Tecnai F20 TEM operated at 200 kV. An aberration-corrected FEI Titan Themis operated at 300 kV was employed to obtain the high-angle annular dark field-STEM (HAADF-STEM) images. The probe convergence semi-angle was either 21.4 or 30 mrad with inner and outer collection angles of 68 and 340 mrad, respectively. GPA was based on the FRWRTools plugin built for DigitalMicrograph [27]. It characterizes lattice distortions relative to the selected reference lattice structure. The positions of Bi^{3+} and Cs^{+} ions in the HAADF-STEM images were identified by Atomap [28], an open-source software package implemented in Python (3.x). Further processing of the ion displacement was also conducted with a script (Supplemental Material [29]) written in Python which includes locating the center positions of two neighboring Cs^{+} ions and drawing an arrow with a color bar to represent displacement of each Bi^{3+} relative to the center of its two neighboring Cs^{+}. The source codes are also available on request.

III. DISCUSSION

A. 180° ferroelectric domain structure with unit-cell-thick domains and sub-1-unit-cell-wide domain walls in free-standing CBNO

We prepare a cross-section sample of free-standing CBNO by exfoliating the synthesized single crystal followed by the standard FIB lift-out procedure (see Methods) for

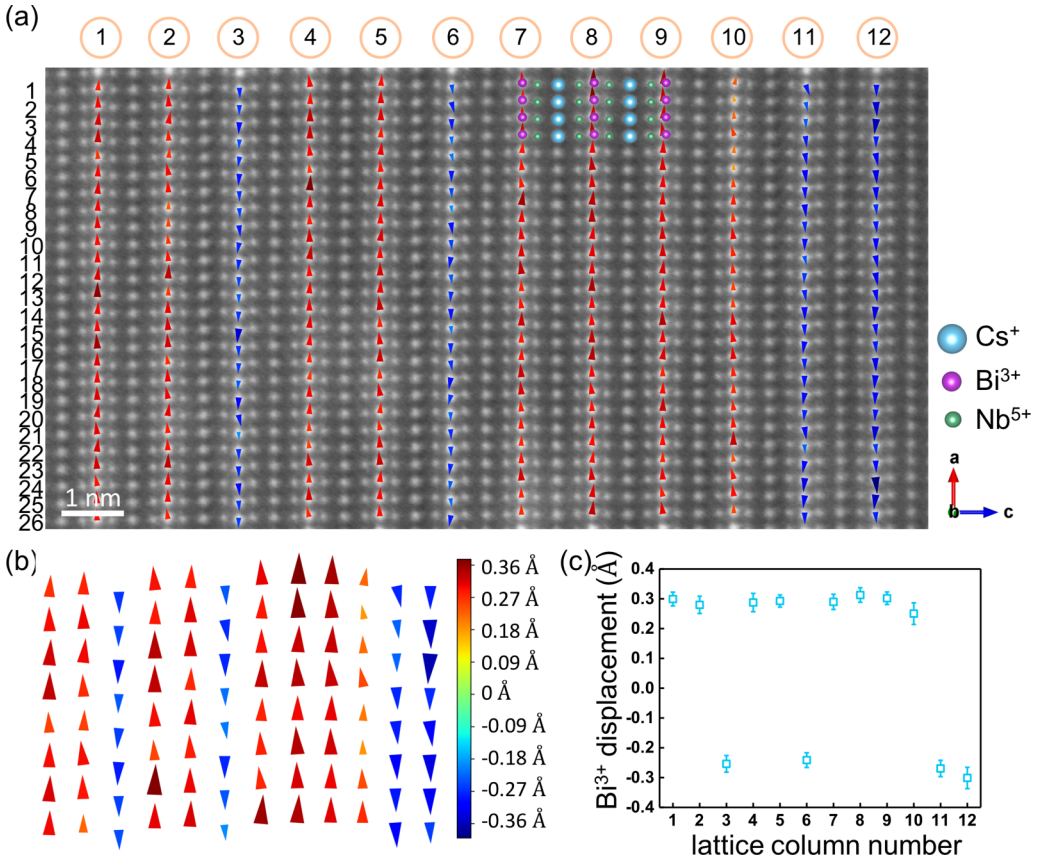

FIG. 1. Unit-cell-thick ferroelectric domains with 180° domain walls. (a) High-angle annular dark field (HAADF) scanning transmission electron microscopy (STEM) image of free-standing $CsBiNb_2O_7$ (CBNO) with zone axis [010]. The sample's orientation is indicated in the lower right corner. 12 lattice columns of Bi^{3+} ions are indexed, as shown on the top of the image, and 26 lattice rows are indexed on the left of the image. The theoretical lattice structure of CBNO is overlaid onto the atomic image. Each arrow indicates the relative displacement of a Bi^{3+} ion with respect to the center of its two neighboring Cs^+ ions. The start position of each arrow is the center of these two neighboring Cs^+ ions. (b) The top 8 rows of arrows in (a) without the STEM image for clarity. The magnitudes of the Bi^{3+} displacement vectors are represented by the arrow area and color. (c) Displacements of Bi^{3+} along the *a* axis relative to the center of two neighboring Cs^+ ions are averaged over each indexed column in (a) and are plotted vs the lattice column number. Error bars represent standard deviation.

high-resolution characterization by Cs-STEM. The projection direction along [010] is chosen such that the *a* axis polarization is parallel to the imaging plane. We overlie the calcuated orthorhombic CBNO crystal structure with similar *a* and *b* lattice constants and stacking direction along the *c* axis onto the HAADF-STEM image of the CBNO sample and find a good structure match, as displayed in Figs. 1(a) and S1(a) in the Supplemental Material [29] (collected from different regions of the sample). The arrows drawn on the STEM images indicate the relative displacements of each Bi^{3+} ion relative to the center of its two neighboring Cs^+ ions (see Methods). The directions of the Bi^{3+} ion displacements are mainly along the polarization axis, namely, the *a* axis. The magnitudes of the Bi^{3+} ion displacements are indicated by the area and color of the arrows, as displayed in Figs. 1(b) and S1(b) in the Supplemental Material [29]. Most displacements are on the order of 0.25–0.35 Å. We also plot the magnitudes of the Bi^{3+} ion displacements along the *a* axis averaged over each lattice column in Figs. 1(c) and S1(c) in the Supplemental Material [29]. The observation of Bi^{3+} ion displacements in the opposite direction along the *a* axis (e.g., blue arrows) demonstrates the presence of neighboring ferroelectric domains with their polarization directions 180° apart, thus, 180° ferroelectric domain walls. We do not observe change of polarization direction within the same layer (with normal axis of *c* axis) of CBNO. The domain wall normal is perpendicular to the polarization directions. We identify ferroelectric domain sizes ranging from ∼1–6 CBNO unit cells along the *c* axis in the HAADF-STEM images, corresponding to ∼1.1–6.9 nm, with average domain width of about 2.2 ± 1.8 nm, which is calculated from 18 180° domains. Such single unit-cell-thick domains could be very promising for nanoscale memory devices. Like most ferroelectric materials, we also detect an abrupt change of the polarization direction across the domain wall in CBNO. This sudden flip of the polarization direction is because a large anisotropy energy would arise in ferroelectrics when the direction of spontaneous polarization deviate from its ferroelectric axis [20]. Thus, in many ferroelectrics, the spontaneous polarization preserves its axis across the domain wall but decreases in magnitude, passes through zero, and then increases its magnitude again in the opposite direction [30,31]. We do not, however, observe a decrease in the polarization magnitude when approaching the domain wall in the CBNO sample, at least within the resolution limits of

the microscope used for this paper, which may indicate a very narrow domain wall, smaller than 1 unit-cell (Figs. 1(c) and S1(c) in the Supplemental Material [29]). The relation between ferroelectric domain size and domain wall width is expressed by Eq. (1) below with detailed derivations presented in the Supplemental Material [29]:

$$\frac{w^2}{\delta t} = \frac{\frac{2}{3}\pi^3\sqrt{\frac{\varepsilon_x}{\varepsilon_z}}}{8.414} \approx 2.45\sqrt{\frac{\varepsilon_x}{\varepsilon_z}}, \tag{1}$$

where w is the domain width, 2δ is the domain wall thickness, t is the sample thickness along the sample polarization direction, ε_z and ε_x are the dielectric constant of a single domain along the polarization axis (CBNO a axis) and perpendicular to the polarization axis (CBNO c axis), respectively.

Such small domain size and narrow domain walls are uncommon in ferroelectrics. We suspect that the small domain size may be due to the small domain wall energy. The elastic energy of the domain wall seems to be negligible because the observed polarization is always close to the spontaneous value. The dipolar energy of the domain wall associated with polarization gradient (i.e., $\frac{\partial P}{\partial x}$, where P is polarization, and x direction is the domain wall normal) [18] is also small because the d spacing along the c direction is large. The smaller domain wall energy makes it energetically favorable to form many small domain strips to reduce the electrostatic energy of the sample.

B. 90° ferroelectric domain structure in free-standing CBNO

A second piece of free-standing CBNO sample was obtained by exfoliating the synthesized CBNO crystal (see Methods) for STEM imaging along the [001] axis. The exfoliated sample is a few micrometers along both the a and b axes. Figure 2(a) shows a HAADF-STEM image of this sample where the horizontal and vertical direction of the image correspond to either a or b axis of CBNO. We perform GPA on Fig. 2(a) and obtain the x direction (horizontal direction) uniaxial strain map ε_{xx}, as displayed in Fig. 2(b). The ε_{xx} strain map shows that the domain on the left has a larger lattice constant along the horizontal direction than that of the domain on the right. These two regions are separated roughly by a black dashed circle to guide the eye.

To resolve the lattice constant relation between the left and the right domains shown in Fig. 2(b), we have conducted the following analysis. First, as shown in Fig. 2(a), we pick up a row of 9 atoms from both the left and right regions (marked by the blue and pink rectangles). Note that each atom observed in the image actually corresponds to an atomic column along the c direction (zone axis). Second, we compare the line profiles (intensity vs horizontal position) of these two rows of atomic columns [Fig. 2(c)]. With the position of the first two atomic columns in each row aligned, we examine the relative displacement of the last two atomic columns from the two rows. We observe that the distance between the first and the last atomic columns of the left row is larger than that of the right row, indicating the left domain has a larger lattice constant in the horizontal direction, which is consistent with the GPA results. The last two peaks [in Fig. 2(c)] from the two rows differ by 0.6 Å. In CBNO, the lattice constant a is 0.07 Å larger than b. Thus, theoretically, the distance between the last two peaks from the two rows should be 0.07 Å×8(0.56 Å), very close to the measured result in Fig. 2(c) from line profiles. With these, we can determine the crystallographic orientations of these two domains [labeled in Figs. 2(a) and 2(b)]: in the left domain, the polarization points in the horizontal direction; in the right domain, the polarization is along the vertical direction. This is similar to the 90° domain wall observed in many classical perovskites.

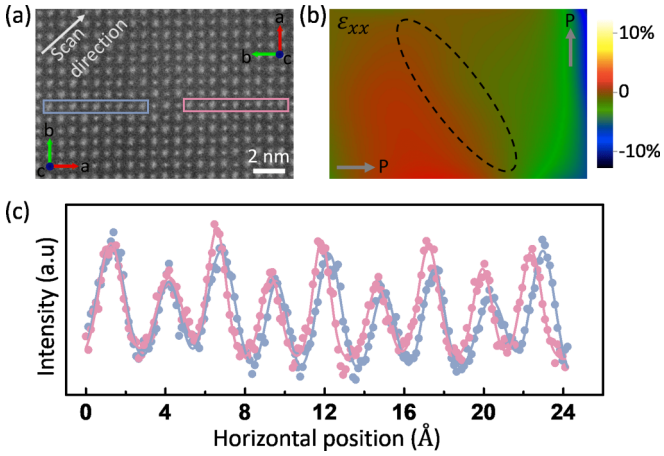

FIG. 2. 90° ferroelectric domain structure characterization. (a) High-angle annular dark field (HAADF) scanning transmission electron microscopy (STEM) image of a free-standing $CsBiNb_2O_7$ (CBNO) film with zone axis [001]. The gray arrow represents the scan direction of the image. (b) The x direction (horizontal direction) strain map ε_{xx} obtained by geometric phase analysis (GPA) performed on the STEM image in (a). The color bar is shown in the range of −10% to 10%. The negative (positive) values in the strain map represent percentage of compression (expansion) of the lattice dimension relative to the reference lattice (not shown), which is selected further away from the domain boundary. The dashed black circle roughly covers the boundary between the left and right domains to guide the eye. (c) Horizontal line profiles along 9 atomic columns (integrated vertically across the width of the atomic row) from the left and right regions of the sample. The color of each curve corresponds to the color of the frame around the selected 9 atomic columns for line profiling shown in (a). The higher intensity peak corresponds to the atomic column (along zone axis) of overlapped Cs^+ and Bi^{3+} ions, while the lower intensity peak corresponds to the atomic column (along zone axis) of Nb^{5+}. The line profiles are fitted by a sum of Gauss functions.

180° domains are also possible in this sample but may be difficult to detect. Since this sample has the c axis of CBNO as its zone axis, in HAADF-STEM images, Bi^{3+} ions are overlapped with Cs^+ ions, as shown in Fig. S2 in the Supplemental Material [29], and thus, the change of Bi^{3+} ion positions due to formation of 180° domains may not be easily resolved.

C. Multiple stacking structures in epitaxial CBNO film on $LaAlO_3$ substrate

We have also grown an epitaxial CBNO film about 50 nm thick on a $LaAlO_3$ substrate by molten-salt assisted synthesis (see Methods). A cross-section of this sample was prepared by FIB (see Methods). Based on the TEM diffraction patterns

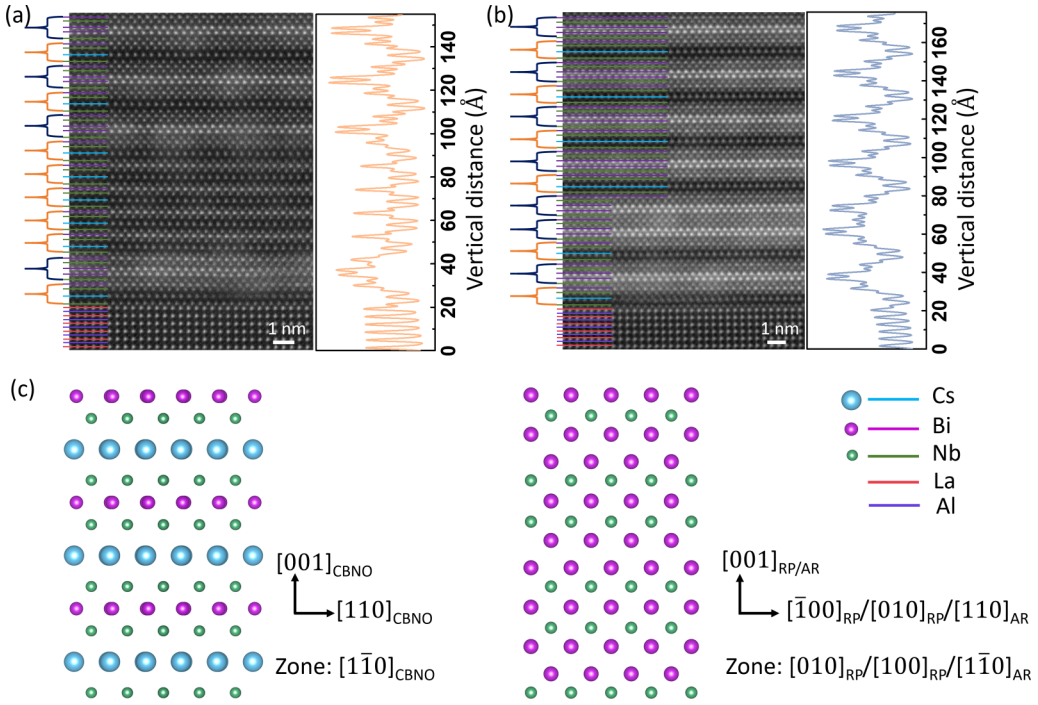

FIG. 3. Multiple stacking structures in the epitaxial $CsBiNb_2O_7$ (CBNO)-$LaAlO_3$ sample. (a) and (b) High-angle annular dark field (HAADF) scanning transmission electron microscopy (STEM) cross-sectional images of the epitaxial CBNO-$LaAlO_3$ sample showing various stacking structures. Different elements are represented by horizontal lines with different colors. Pink lines represent Bi, green Nb, blue Cs, red La, and purple Al. (c) Left panel shows the structure of CBNO marked by the orange brackets in (a) and (b). Right panel shows the structure marked by the dark blue brackets in (a) and (b).

obtained from this cross-section sample, as shown in Fig. S3 in the Supplemental Material [29], we determine that the epitaxial relation is surface normal $LaAlO_3$ [001]//CBNO [001] and $LaAlO_3$(100)//CBNO(110). Here, $LaAlO_3$ is indexed with pseudocubic notation for convenience. We obtain HAADF-STEM images [Figs. 3(a) and 3(b)] from different locations of the CBNO-$LaAlO_3$ cross-section sample. Since the intensity of an atomic column in HAADF-STEM is related to the atomic number of the element and the number of atoms in the column [32], we identify each atomic column (along the projections axis) based on its contrast in STEM images. Overlaid on the STEM images are horizontal lines whose color denotes the elemental species of that layer in the crystalline structure. To characterize the stacking structures of the film, we plot line profiles along the film growth direction (perpendicular to the film-substrate interface) next to each STEM image. Both the HAADF-STEM images and their corresponding line profiles reveal varied stacking sequences in the epitaxial film. The stacking structure marked by the orange bracket corresponds to the nominally correct stacking sequence of CBNO, also displayed in the left in Fig. 3(c), which alternates between single rows of Cs and Bi atoms separated by rows of Nb. By comparison, the stacking structure marked by the dark blue bracket shows a different sequence, where a row of Cs ions is missing and replaced instead by two rows of Bi ions present next to each other. This stacking structure may be assigned to either an Aurivillius (AR) phase consisting of $[Bi_3Nb_2O_9]^+$ with zone axis [1$\bar{1}$0], or a Ruddlesden–Popper (RP) phase of $[Bi_3Nb_2O_7]^{5+}$ with zone axis [010] or [100], as shown in the right in Fig. 3(c). The charge neutrality condition might be maintained by cation vacancies or varying cation valences [33]. The loss of Cs^+ in CBNO films grown on $LaAlO_3$ substrate but not in free-standing CBNO may be due to the nonuniform solution of the precursors used in molten-salt assisted synthesis (see Methods). $LaAlO_3$ substrate is at the bottom of the precursors solution, where there are higher concentrations of Bi^{3+} and Nb^{5+} ions than Cs^+ ions (see Methods). So CBNO grown on $LaAlO_3$ substrate has a deficiency of Cs^+. On the contrary, free-standing CBNO is grown in the uniform region of the solution with optimized ions ratio, so no ion deficiency is observed. We also find another stacking structure at the film-substrate interface shown in Fig. S4 in the Supplemental Material [29]. Existence of multiple stacking structures are commonly reported in many other layered oxides [33–36].

We then take a closer look at the interface [Figs. 4(a) and 4(b)] between CBNO and $LaAlO_3$. We observe that the second row of Nb (away from the CBNO-$LaAlO_3$ interface) misses a column of Nb ions along the zone axis of the sample, signaling a misfit dislocation at the interface between the first and the second row of Nb. To perform GPA on the strain field of this dislocation, we select a dislocation-free region as a reference and characterize the lattice distortions around the interfacial dislocation relative to the reference region. Thus, the reference region needs to have the same lattice structure as the interfacial layers where dislocation occurs. The region marked by the cyan rectangle in Fig. 4(a) has a crystal structure of CBNO, which matches the unit-cell-thick CBNO interface layer and is thus used as the GPA reference. The region in Fig. 4(b) also shows a single CBNO layer at

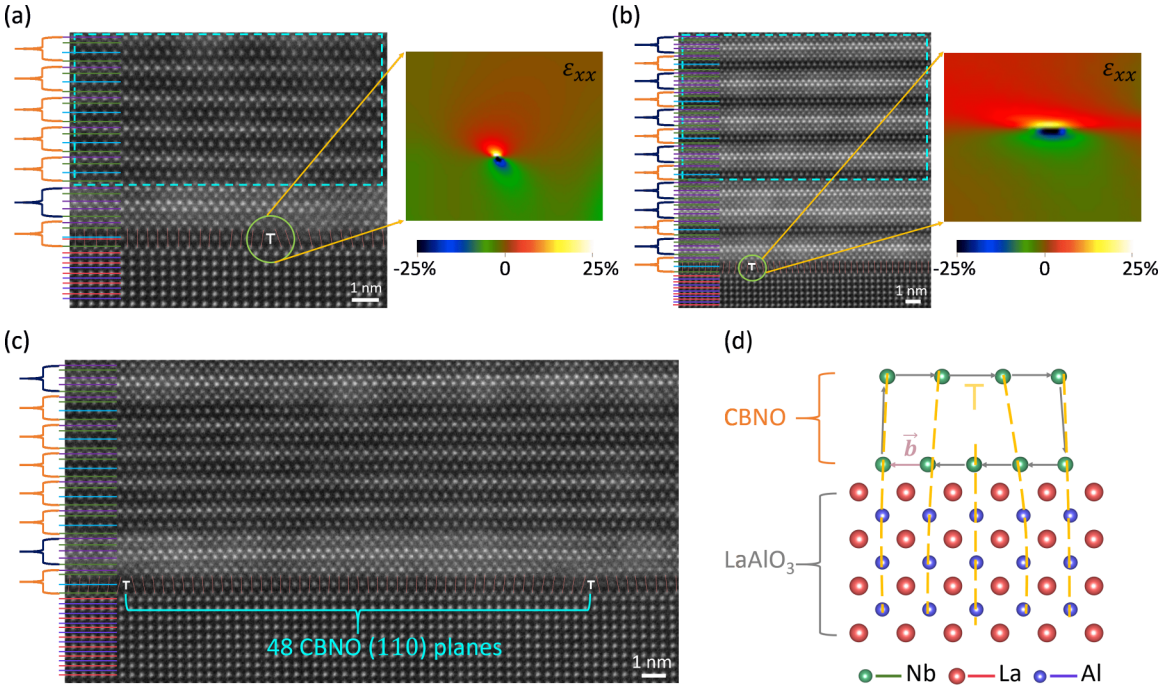

FIG. 4. Interfacial dislocations in the epitaxial $CsBiNb_2O_7$ (CBNO)-$LaAlO_3$ sample. (a) High-angle annular dark field (HAADF) scanning transmission electron microscopy (STEM) image of the interface taken from the image in Fig. 3(a). An interfacial dislocation is indicated at the film-substrate interface. The pink lines connect the positions of two Nb planes nearest to the interface. Same with Fig. 3, the orange brackets mark the structure of CBNO, and the dark blue bracket marks the structure resembling either Aurivillius (AR) or Ruddlesden–Popper (RP) phase. The x direction (horizontal direction) strain map ε_{xx} around the dislocation is shown on the right of the HAADF-STEM image. (b) Zoomed-in HAADF-STEM image at the interface corresponding to the original image in Fig. 3(b). The pink lines connect the positions of two Nb planes nearest to the interface. Same with Fig. 3, the orange brackets mark the structure of CBNO, and the dark blue brackets mark the structure resembling either AR or RP phase. The x direction (horizontal direction) strain map ε_{xx} around the dislocation is shown on the right. For both strain maps, the color bars are shown in the range of -25% to 25%. Positive (negative) values in the strain maps represent tensile (compressive) lattice distortions relative to their respective reference region selected by the cyan rectangle. (c) HAADF-STEM image at the interface of CBNO-$LaAlO_3$ where two successive dislocations in CBNO are observed. The pink lines connect the positions of two Nb planes nearest to the interface. Same with Fig. 3, the orange brackets mark the structure of CBNO, and the dark blue brackets mark the structure resembling either AR or RP phase. (d) Atomic model illustrating the interfacial dislocation observed in the STEM images in (a)–(c). The Burgers vector $\tilde{\mathbf{b}}$ is drawn on the model. 3-unit-cell-thick of $LaAlO_3$ substrate (only Al and La atoms for simplicity) and 1-unit-cell-thick of CBNO film (only Nb atoms for simplicity) are shown. The Burgers vector $\tilde{\mathbf{b}}$ is also drawn on the model.

the interface, but no nearby large regions with continuous CBNO stacking structure to serve as the reference can be found. Instead, we combine the interfacial CBNO unit with the stacking unit right above it [which resembles the AR or RP phase shown in Fig. 3(c)] as a new structure unit. The structure of this composite unit is identical to the region marked by the cyan rectangle in Fig. 4(b), which can thus be used as a GPA reference for this image. Using these respective references, we obtain x direction (horizontal direction) uniaxial strain maps ε_{xx} [37] for each of the interfacial dislocations, shown at the right of the corresponding STEM images. The lattice misfit at the interface between CBNO (110) [$d_{(110)} = 3.88$ Å] and $LaAlO_3$ (100) [$d_{100} = 3.79$ Å] is about 2.4%. Based on this misfit, we estimate interfacial dislocations to occur every 42 planes of CBNO (110) to fully relax the lattice strain. Indeed, we observe two successive dislocations separated by 48 CBNO (110) planes in a HAADF-STEM image [Fig. 4(c)]. An atomic model showing the lattice structure of this interfacial dislocation is displayed in Fig. 4(d). Because the d spacing of CBNO (110) is larger than that of $LaAlO_3$ (110), the epitaxial CBNO is under compressive strain at the interface (corresponding to the compressive region in the ε_{xx} strain maps), as shown by the smaller in-plane distance between ions in the Nb atomic columns nearest to the interface. In the second nearest row of Nb to the interface, the compressive strain is released by reducing an atomic column of Nb. The in-plane ion spacings are slightly larger than the strain-free region due to a missing Nb column (corresponding to the tensile region in the ε_{xx} strain maps).

IV. CONCLUSIONS

In quasi-2D free-standing CBNO films, we have discovered 180° domains that are a single unit-cell thick. We have also revealed the existence of 90° domains by characterizing the change in domain orientations across the domain wall. In the epitaxial CBNO film grown on a $LaAlO_3$ substrate, we have found multiple stacking structures and interfacial dislocations, highlighting the role of the substrate on the structure of the quasi-2D film. Our understanding of the domain structure of the quasi-2D ferroelectric material may suggest material categories to achieve unit-cell-thick domain

structures and shed light on promising material solutions for next-generation microelectronic devices, such as nonvolatile high-density memories and synaptic devices.

Raw data and codes are available upon reasonable request.

ACKNOWLEDGMENTS

Y.G. and J.S. acknowledge the Air Force Office of Scientific Research under Award No. FA9550-18-1-0116. L.Z. and J.S. acknowledge the NYSTAR Focus Center under Award No. C150117. This paper is supported by the National Science Foundation [Platform for the Accelerated Realization, Analysis, and Discovery of Interface Materials (PARADIM)] under Cooperative Agreement No. DMR-1539918 and made use of the Cornell Center for Materials Research (CCMR) Shared Facilities, which are supported through the NSF MRSEC Program (No. DMR-1719875). The FEI Titan Themis 300 was acquired through No. NSF-MRI-1429155, with additional support from Cornell University, the Weill Institute, and the Kavli Institute at Cornell. This paper is also partially supported by the National Science Foundation under Awards No. 2024972, No. 2031692, and No. 1916652.

J.S. conceived the project. L.Z. provided free-standing and epitaxial CBNO samples. Y.G. carried out FIB preparation of cross-section samples and TEM characterization. B.G. performed Cs-STEM characterization. Y.G. carried out GPA. Y.C. and Y.G. completed the Python script for characterizing ion positions and displacements on STEM images. Y.G. wrote the paper. All the authors discussed the results and commented on the manuscript.

[1] N. Setter and R. Waser, Electroceramic materials, Acta Mater. **48**, 151 (2000).

[2] J. F. Scott, Applications of modern ferroelectrics, Science **315**, 954 (2007).

[3] M. Dawber, K. M. Rabe, and J. F. Scott, Physics of thin-film ferroelectric oxides, Rev. Mod. Phys. **77**, 1083 (2005).

[4] T. Miyamoto, H. Yada, H. Yamakawa, and H. Okamoto, Ultrafast modulation of polarization amplitude by terahertz fields in electronic-type organic ferroelectrics, Nat. Commun. **4**, 2586 (2013).

[5] C. L. Jia, K. W. Urban, M. Alexe, D. Hesse, and I. Vrejoiu, Direct observation of continuous electric dipole rotation in flux-closure domains in ferroelectric Pb(Zr, Ti)O_3, Science **331**, 1420 (2011).

[6] M. J. Polking, M. G. Han, A. Yourdkhani, V. Petkov, C. F. Kisielowski, V. V. Volkov, Y. Zhu, G. Caruntu, A. P. Alivisatos, and R. Ramesh, Ferroelectric order in individual nanometre-scale crystals, Nat. Mater. **11**, 700 (2012).

[7] M. K. Kim and J. S. Lee, Ferroelectric analog synaptic transistors, Nano Lett. **19**, 2044 (2019).

[8] R. Guo, L. You, Y. Zhou, Z. S. Lim, X. Zou, L. Chen, R. Ramesh, and J. Wang, Non-volatile memory based on the ferroelectric photovoltaic effect, Nat. Commun. **4**, 1990 (2013).

[9] K. Chang, J. Liu, H. Lin, N. Wang, K. Zhao, A. Zhang, F. Jin, Y. Zhong, X. Hu, W. Duan, and Q. Zhang, Discovery of robust in-plane ferroelectricity in atomic-thick SnTe, Science **353**, 274 (2016).

[10] D. Ji, S. Cai, T. R. Paudel, H. Sun, C. Zhang, L. Han, Y. Wei, Y. Zang, M. Gu, Y. Zhang, W. Gao, H. Huyan, W. Guo, D. Wu, Z. Gu, E. Y. Tsymbal, P. Wang, Y. Nie, and X. Pan, Freestanding crystalline oxide perovskites down to the monolayer limit, Nature **570**, 87 (2019).

[11] C. Cui, W. J. Hu, X. Yan, C. Addiego, W. Gao, Y. Wang, Z. Wang, L. Li, Y. Cheng, P. Li, X. Zhang, H. N. Alshareef, T. Wu, W. Zhu, X. Pan, and L. J. Li, Intercorrelated in-plane and out-of-plane ferroelectricity in ultrathin two-dimensional layered semiconductor In_2Se_3, Nano Lett. **18**, 1253 (2018).

[12] F. Liu, L. You, K. L. Seyler, X. Li, P. Yu, J. Lin, X. Wang, J. Zhou, H. Wang, H. He, S. T. Pantelides, W. Zhou, P. Sharma, X. Xu, P. M. Ajayan, J. Wang, and Z. Liu, Room-temperature ferroelectricity in $CuInP_2S_6$ ultrathin flakes, Nat. Commun. **7**, 12357 (2016).

[13] Y. Zhou, D. Wu, Y. Zhu, Y. Cho, Q. He, X. Yang, K. Herrera, Z. Chu, Y. Han, M. C. Downer, H. Peng, and K. Lai, Out-of-plane piezoelectricity and ferroelectricity in layered alpha-In_2Se_3 nanoflakes, Nano Lett. **17**, 5508 (2017).

[14] C. Zheng, L. Yu, L. Zhu, J. L. Collins, D. Kim, Y. Lou, C. Xu, M. Li, Z. Wei, Y. Zhang, and M. T. Edmonds, Room temperature in-plane ferroelectricity in van der Waals In_2Se_3, Sci. Adv. **4**, eaar7720 (2018).

[15] J. A. Brehm, S. M. Neumayer, L. Tao, A. O'Hara, M. Chyasnavichus, M. A. Susner, M. A. McGuire, S. V. Kalinin, S. Jesse, P. Ganesh, S. T. Pantelides, P. Maksymovych, and N. Balke, Tunable quadruple-well ferroelectric van der Waals crystals, Nat. Mater. **19**, 43 (2020).

[16] G. Catalan, H. Bea, S. Fusil, M. Bibes, P. Paruch, A. Barthelemy, and J. F. Scott, Fractal Dimension and Size Scaling of Domains in Thin Films of Multiferroic $BiFeO_3$, Phys. Rev. Lett. **100**, 027602 (2008).

[17] A. S. Everhardt, S. Matzen, N. Domingo, G. Catalan, and B. Noheda, Ferroelectric domain structures in low-strain $BaTiO_3$, Adv. Electron. Mater. **2**, 1500214 (2016).

[18] G. Catalan, J. Seidel, R. Ramesh, and J. F. Scott, Domain wall nanoelectronics, Rev. Mod. Phys. **84**, 119 (2012).

[19] G. Catalan, J. F. Scott, A. Schilling, and J. M. Gregg, Wall thickness dependence of the scaling law for ferroic stripe domains, J. Phys.: Condens. Matter **19**, 022201 (2007).

[20] W. Kanzig, *Solid State Physics* (Academic Press, New York, 1957).

[21] C. J. Fennie and K. M. Rabe, Ferroelectricity in the Dion–Jacobson $CsBiNb_2O_7$ from first principles, Appl. Phys. Lett. **88**, 262902 (2006).

[22] N. A. Benedek, Origin of ferroelectricity in a family of polar oxides: the Dion–Jacobson phases, Inorg. Chem. **53**, 3769 (2014).

[23] C. Chen, H. Ning, S. Lepadatu, M. Cain, H. Yan, and M. J. Reece, Ferroelectricity in Dion–Jacobson $ABiNb_2O_7$ (A = Rb, Cs) compounds, J. Mater. Chem. C **3**, 19 (2015).

[24] H. Djani, A. C. Garcia-Castro, W.-Y. Tong, P. Barone, E. Bousquet, S. Picozzi, and P. Ghosez, Rationalizing and engineering Rashba spin-splitting in ferroelectric oxides, npj Quantum Mater. **4**, 51 (2019).

[25] C. Autieri, P. Barone, J. Sławińska, and S. Picozzi, Persistent spin helix in Rashba–Dresselhaus ferroelectric $CsBiNb_2O_7$, Phys. Rev. Mater. **3**, 084416 (2019).

[26] S. Pendse, J. Jiang, Y. Guo, L. Zhang, Z. Chen, Z. Lu, Y. Wang, Y. Hu, S. Li, J. Feng, T.-M. Lu, Y.-Y. Sun, and J. Shi, Unit-cell-thick oxide synthesis by film-based scavenging, J. Phys. Chem. C **124**, 8394 (2020).

[27] M. J. Hÿtch, E. Snoeck, and R. Kilaas, Quantitative measurement of displacement and strain fields from HREM micrographs, Ultramicroscopy **74**, 131 (1998).

[28] M. Nord, P. E. Vullum, I. MacLaren, T. Tybell, and R. Holmestad, Atomap: a new software tool for the automated analysis of atomic resolution images using two-dimensional Gaussian fitting, Adv. Struct. Chem. imaging **3**, 9 (2017); http://atomap.org.

[29] See Supplemental Material at http://link.aps.org/supplemental/10.1103/PhysRevMaterials.5.044403 for materials structure analysis, derivation of the relation between domain width and domain wall width, plots of electric fields inside and outside a ferroelectric plate sample, and Python script for characterization of ion position and displacements. Supplemental Material includes additional Refs. [38–47].

[30] K. Holsgrove, Transmission electron microscopy study of domains in ferroelectrics, Ph.D. thesis, Queen's University Belfast, 2017.

[31] C. L. Jia, S. B. Mi, K. Urban, I. Vrejoiu, M. Alexe, and D. Hesse, Atomic-scale study of electric dipoles near charged and uncharged domain walls in ferroelectric films, Nat. Mater. **7**, 57 (2008).

[32] S. J. Pennycook and D. E. Jesson, High-resolution Z-contrast imaging of crystals, Ultramicroscopy **37**, 14 (1991).

[33] M. A. Zurbuchen, W. Tian, X. Q. Pan, D. Fong, S. K. Streiffer, M. E. Hawley, J. Lettieri, Y. Jia, G. Asayama, S. J. Fulk, D. J. Comstock, S. Knapp, A. H. Carim, and D. G. Schlom, Morphology, structure, and nucleation of out-of-phase boundaries (OPBs) in epitaxial films of layered oxides, J. Mater. Res. **22**, 1439 (2011).

[34] T. Nakajima, T. Tsuchiya, and D. Viehland, Ion-exchange protonation and enhanced seed layer property of uniaxially grown $RbLaNb_2O_7$ thin films on glass substrates, J. Am. Ceram. Soc. **95**, 573 (2012).

[35] G. Stone, C. Ophus, T. Birol, J. Ciston, C. H. Lee, K. Wang, C. J. Fennie, D. G. Schlom, N. Alem, and V. Gopalan, Atomic scale imaging of competing polar states in a Ruddlesden–Popper layered oxide, Nat. Commun. **7**, 12572 (2016).

[36] Y. Yan, M. M. Al-Jassim, Z. Xu, X. Lu, D. Viehland, M. Payne, and S. J. Pennycook, Structure determination of a planar defect in $SrBi_2Ta_2O_9$, Appl. Phys. Lett. **75**, 1961 (1999).

[37] Y. Han, K. Nguyen, M. Cao, P. Cueva, S. Xie, M. W. Tate, P. Purohit, S. M. Gruner, J. Park, and D. A. Muller, Strain mapping of two-dimensional heterostructures with subpicometer precision, Nano Lett. **18**, 3746 (2018).

[38] A. Kopal, T. Bahnik, and J. Fousek, Domain formation in thin ferroelectric films: the role of depolarization energy, Ferroelectrics **202**, 267 (1997).

[39] J. L. Bjorkstam and R. E. Oettel, 180° domain formation in ferroelectrics with shorted electrodes, Phys. Rev. **159**, 427 (1967).

[40] T. Mitsui and J. Furuichi, Domain structure of Rochelle salt and KH_2PO_4, Phys. Rev. **90**, 193 (1953).

[41] H. Mueller, Properties of Rochelle salt, Phys. Rev. **57**, 829 (1940).

[42] H. Mueller, Properties of Rochelle salt. III, Phys. Rev. **58**, 565 (1940).

[43] V. A. Zhirnov, A contribution to the theory of domain walls in ferroelectrics, Sov. Phys. JETP **35**, 822 (1959).

[44] R. J. Goff, D. Keeble, P. A. Thomas, C. Ritter, F. D. Morrison, and P. Lightfoot, Leakage and proton conductivity in the predicted ferroelectric $CsBiNb_2O_7$, Chem. Mater. **21**, 1296 (2009).

[45] G. Gou and J. Shi, Piezoelectricity enhancement in Dion–Jacobson $RbBiNb_2O_7$ via negative pressure, Europhys. Lett. **108**, 67006 (2014).

[46] M. C. Knapp, Investigations into the structure and properties of ordered perovskites, layered perovskites, and defect pyrochlores, Ph.D. thesis, Ohio State University, 2006.

[47] B. W. Li, M. Osada, T. C. Ozawa, and T. Sasaki, $RbBiNb_2O_7$: a new lead-free high-Tc ferroelectric, Chem. Mater. **24**, 3111 (2012).